Click to view slide presentation

[EA]Quantitative Calibration of Hyperspectral Core Imaging Data: A New Method for Producing Continuous, High-Resolution Mineralogical Characterization of Cores from Both Conventional and Unconventional Reservoirs*

James Greene[1], Tobi H. Kosanke[2], and Paul Linton[3]

Search and Discovery Article #42444 (2019)**
Posted September 9, 2019

*Adapted from extended abstract prepared in conjunction with oral presentation given at 2019 AAPG Annual Convention and Exhibition, San Antonio, Texas, May 19-22, 2019
 DOI:10.1306/42444Greene2019

[1]CoreSolution Technologies, Reno, NV (james.greene@nutechenergy.com)
[2]Consultant, Houston, TX
[3]TerraCore, Reno, NV

Abstract

Hyperspectral imaging (HI) of core involves utilization of non-destructive, infrared spectroscopy to capture mineralogical and textural information of the slabbed face of a core. Spectral information obtained from two spectrometers, one that detects energy within the short-wave infrared (SWIR) spectrum and the other within the long-wave infrared (LWIR) spectrum, is co-registered to identify the in-situ minerals present on the core face including tectosilicates such as quartz and feldspar, which cannot be detected in the SWIR or very-near infrared (VNIR) ranges. The spectral data are acquired, using specialized high-resolution lenses, at a spatial resolution of 300 to 500 microns per pixel, allowing identification of thin laminae and subtle sedimentological features in cores from both conventional and unconventional reservoirs. This level of resolution also enables integration of the relatively continuous HI data with information obtained from more spatially discrete measurements such as X-ray diffraction (XRD) data, thin section petrography, and scanning electron microscopy (SEM) to facilitate upscaling of those fine-scale data to core and wireline log scales.

Many standard HI analyses involve interpretive or spectral-matching classifications of waveforms to deliver qualitative mineralogical information. Although a variety of spectral un-mixing algorithms can be used to infer mineralogy in a more quantitative manner, the un-mixing techniques are impacted by the non-linearity and spectral variability of mineral mixing. In this study, analytic models were developed to calibrate spectral classifications using XRD data as control points. Forward modeling was used to validate the fit between the measured and predicted property values. This methodology was successfully applied using HI data obtained on several cores from both conventional and unconventional formations.

Introduction

Hyperspectral core imaging involves a method of non-destructive, infrared spectroscopy to capture mineralogical and textural information of the slabbed face of a core (Kosanke et al., 2017). The application of this technology to core analysis evolved from an origin in multispectral, remote sensing programs where it was used to acquire satellite imagery of Earth (Bernstein, 1976). The mining industry was quick to implement the use of visible near-infrared (VNIR) and short-wave infrared (SWIR) in airborne systems for exploration (Vane and Goetz, 1988; Bierwirth et al., 2002; Plaza et al., 2009; Taranik and Aslett, 2009; Murphy and Monteiro, 2013). Other industries, such as agriculture, pharmaceuticals, homeland security, medicine, recycling, food, forensics, and art have also adopted hyperspectral analysis in a variety of applications (ElMasry and Sun, 2010; Sun, 2010; Marshall, 2011; Edelman et al., 2012; Lu and Fei, 2014; Cucci et al., 2016). Technological advances in the last few decades have enabled the collection of data at higher spatial and spectral resolutions (Kurz et al., 2008; Monteiro et al., 2009; Kurz et al., 2011; Murphy and Monteiro, 2013; Kosanke et al., 2017). In 2007, VNIR-SWIR hyperspectral imaging was implemented into core analysis workflows for the mining industry with notable success.

Although valuable for the mining industry, HI systems utilizing the VNIR–SWIR spectral regions had limited applicability for hydrocarbon reservoirs due to the inability for certain minerals to be uniquely detected, including quartz and feldspar (Hunt et al., 1973). The introduction of long-wave infrared (LWIR) data collection for core imaging became a significant technical advancement to allow the identification of tectosilicate mineral species, which were formerly aspectral in the VNIR-SWIR (Kosanke et al., 2017). The addition also facilitates the acquisition of improved spectral information from dark lithologies which exhibit low reflectance in the VNIR-SWIR. The integration of spectrometers using specialized lenses provides the ability to detect a comprehensive range of minerals including carbonate, clay, tectosilicate, and sulfate species at a high resolution of 300-500 micron pixels. The SWIR also has hydrocarbon detection capabilities to augment the inorganic characterization.

Data and Methodology

Hyperspectral image data was acquired using an integrated system located at ALS Oil & Gas Laboratories in Houston, TX and operated in partnership with TerraCore. The system includes the sequencing of two infrared spectrometers to capture both the long-wave and short-wave infrared regions. A visible light, RGB, camera is also utilized to provide a natural color image for reference.

The SWIR spectrometer collects 288 bands of data between 1000 and 2500 nm, at 5.6 nm sampling rate and 9 nm spectral resolution. The LWIR spectrometer collects 96 bands of data between 7700 and 12300 nm, at 48 nm sampling rate and 100 nm spectral resolution. Data are collected at a high spatial resolution of approximately 400 microns per pixel for the infrared spectrometers and 120 microns per pixel for the RGB camera. The pixel resolution captured for these datasets reduces the degree of mineral mixing and provides more detailed mapping for thin bedding and laminations (Browning and Kosanke, 2016).

Reference material data (Spectralon for the SWIR and brushed aluminum for the LWIR) are acquired along with dark current measurements for each core image. Dark current measurements account for the noise generated by the temperature difference between the environment and the hyperspectral camera (Manea and Calin, 2015).

Following data acquisition, core masking processes are used to extract the desired pixels for analysis from the background, open fractures, and uneven surfaces. This masking procedure allows the image analysis routines to exclude outlier and noise-attributing data. Due to the size and dimensionality of the acquired image dataset, an artificial neural network computational model is then utilized to separate the dataset into classifications that are spectrally and spatially significant. The unsupervised self-organizing map (SOM) classification algorithm is applied with specific wavelet features being designated as endmember variables. SOM has proven to be an effective method of classifying nonlinear data with a large number of variables by calculating the minimum distances between data points (Al Ibrahim, 2014). Every masked pixel on the core surface is associated with a SOM class from each infrared spectrometer, with each SOM class representing a variation in the spectral response. Within the spectrum of each SOM classification, there are diagnostic absorption and reflectance features that can be qualitatively interpreted to facilitate mineral identification, elemental substitutions, crystallinity, and relative grain sizes. Although spectral reference libraries are available for pure minerals, the mineral mixtures that exist in fine-grained sedimentary reservoirs will produce waveforms that exhibit spectral variability and non-linear behavior (Bioucas-Dias et al., 2012).

Because spectral imaging produces a generally qualitative dataset, a “ground truth” dataset is required to calibrate the unknown SOM-derived classes to quantifiable mineral abundances. For this illustration of our modeling approach, we utilized XRD data, though other quantitative datasets have the potential to be used. Due to the degree of mineral mixing within individual pixels, our model designates the entire spectrum as input variables rather than targeting individual, diagnostic wavelets. At each location on the core face for which a sample was obtained for XRD analysis, the co-existing series of SOM data are associated to build a large, multivariate system of equations. Additional constraints are implemented to prevent the model from producing a sum of mineral abundances greater than unity (100%) and individual mineral species greater than their mineral group. With the system of equations and constraints built, a series of regressions are performed to minimize the sum of squared differences and/or sum of squared relative errors between the known mineral abundance and calculated mineral abundance for various mineral groups.

The solved variable coefficients can then be applied to the full dataset for continuous, calculated mineralogy at all depths along the imaged interval.

Results and Discussion

Our model was individually implemented on slabbed, legacy cores from the Austin Chalk, Bone Spring Shale, Eagle Ford, and Wilcox formations. Each cored formation contained approximately 250 feet of cumulative footage with occasional gaps due to testing and removal. The XRD datasets for each formation were sourced from various laboratories. Though not by design, the differences in the XRD data sourcing helps to evaluate whether the model can be applied on other legacy core and external datasets. Each uncalibrated HI dataset was calibrated using a subset of XRD data points and then compared the forward modeled results from the full XRD dataset.

The modeled hyperspectral mineral abundances were plotted against the measured XRD mineral abundances in Figure 1, Figure 2, and Figure 3. For each, a best-fit linear trend was generated to better understand the accuracy and precision of the calibration. To start, the linear equations show positive relationships between the model (x) and the known values (y) indicating that the SOM classifications are capturing the high and low limits of the XRD values. The R^2 values, which are a statistical measure of how close each calibration point (x, y) is to the best-fit

linear trend, also suggest the model fits the data with minimal scatter. In general, the closer the R^2 value is to 1, the better the model fits the data.

The accuracy of the calibrated results is a function of both the number of calibration points used and the range of SOM classifications that are sampled by XRD. The higher number of SOM classifications that the calibration points comprise, the better the calibration will be. To aid the calibration workflow, the uncalibrated SOM data should be used to guide the selection of samples for XRD analysis. For this study, the optimal number of samples for calibration was found to approximately one XRD sample per 10 to 15 feet of core.

The primary assumptions associated with this model are:

- All of the minerals reported in the XRD data are present in the SOM classes. The fit between the calibration results and XRD values indicates that the SOM classification is an effective approach for capturing the presence of major and minor minerals; however, its ability to detect trace minerals requires further investigation.

- The hyperspectral image data and the associated XRD calibration point represent the same bulk rock. This strongly depends on the XRD sampling technique, particularly if there is a mineralogical difference between the location sampled for XRD and the imaged core surface.

- The external dataset used to calibrate the spectral data is accurate. The accuracy of XRD data in particular will vary by laboratory, and is a function of sample preparation, instrumentation, and analytical technique (Bish and Chipera, 1988).

The calibration of hyperspectral SOM classification data to XRD mineral abundances also enabled continuous single mineral logs to be produced (Figure 4). Although these logs have a degree of uncertainty associated with their calibrated values, the addition of high-resolution, continuous mineralogical trends with depth adds significant understanding compared to discrete XRD point analyses. The logs can also be plotted alongside petrophysical logs, albeit at a much higher resolution, to assist in the upscaling of other fine-scale, discrete datasets (Kosanke and Chen, 2017). The high resolution of the hyperspectral-derived mineralogy compared to the log-derived mineralogy is evident by the capture of thin laminae and inter-beds (Browning and Kosanke, 2016).

Conclusions

Although the image products (mineral maps) generated by hyperspectral imaging provide textural understanding of the mineralogical variations and assemblages observed on the slabbed core surface, there is a need to transform spectrally-derived mineralogical information into quantitative data for calculation and modeling purposes and for input of mineralogy as curves into petrophysical software.

The calibration of hyperspectral imaging from the short-wave infrared (SWIR) and long-wave infrared (LWIR) spectra provides a valuable step towards quantifying core mineralogy at a high-resolution. The addition of continuous mineralogical trends from our hyperspectral-imaging-

derived (SWIR + LWIR) model adds significant value to discrete XRD point analyses, and can likely be improved with continued development. The mid-wave infrared region (MWIR) is an area for future investigation, due to its sensitivity to both hydrocarbons and mineral species, to improve our model for comprehensive organic and inorganic characterization.

References Cited

Al Ibrahim, M.A.H., 2014, Multi-Scale Sequence Stratigraphy, Cyclostratigraphy, and Depositional Environment of Carbonate Mudrocks in the Tuwaiq Mountain and Hanifa Formations, Saudi Arabia: M.S. Thesis, Colorado School of Mines, Golden, CO, 181 p.

Bernstein, R., 1976, Digital Image Processing of Earth Observation Sensor Data: IBM Journal of Research Development, v. 20, p. 40-57.

Bierwirth, P., 2002, Hyperspectral Mapping of Mineral Assemblages Associated with Gold Mineralization in the Central Pilbara, Western Australia: Economic Geology, v. 97/4, p. 819-826. doi.10.2113/97.4.819

Bioucas-Dias, J., A. Plaza, N. Dobigeon, M. Parente, Q. Du, P. Gader, and J. Chanussot, 2012, Hyperspectral Unmixing Overview: Geometrical, Statistical, and Sparse Regression-Based Approaches: IEEE Journal of Selected Topics in Applied Earth Observations and Remote Sensing, v. 5, p. 354-379.

Bish, D.L., and S.J. Chipera, 1988, Problems and Solutions in Quantitative Analysis of Complex Mixtures by X-ray Powder Diffraction: Advances in X-ray Analysis v. 31, p. 295-308.

Browning, D., and T. Kosanke, 2016, Mineral Mapping of Core using Combined High-resolution SWIR and LWIR Sensors: Presentation, Geological Remote Sensing Group, London, UK, December 2016.

Cucci, C., J.K. Delaney, and M. Picollo M, 2016, Reflectance Hyperspectral Imaging for Investigation of Works of Art: Old Master Paintings and Illuminated Manuscripts: Accounts of Chemical Research, v. 49/10, p. 2070-2079.

Edelman, G., E. Gaston, T. Van Leeuwen, P. Cullen, and M. Aalders, 2012, Hyperspectral Imaging for Non-contact Analysis of Forensic Traces: Forensic Science International, v. 223, p. 28-39.

ElMasry, G., and D.-W. Sun, 2010, Principles of Hyperspectral Imaging Technology, *in* D.-W. Sun (ed.), Hyperspectral Imaging for Food Quality Analysis and Control: Academic Press, Elsevier, London, p. 3-43.

Herrmann, W., M. Blake, M. Doyle, D. Huston, J. Kamprad, N. Merry, and S. Pontual, 2001, Short Wavelength Infrared (SWIR) Spectral Analysis of Hydrothermal Alteration Zones Associated with Base Metal Sulfide Deposits at Rosebery and Western Tharsis, Tasmania, and Highway-Reward, Queensland: Economic Geology, v. 96, p. 939-955.

Hunt, G.R., J.W. Salisbury, and C.J. Lenhoff, 1973, Visible and Near Infrared Spectra of Minerals and Rocks. VI. Additional Silicates: Modern Geology, v. 4, p. 85-106.

Kosanke T.H., and J. Chen, 2017, Hyperspectral Imaging: Geological and Petrophysical Applications to Reservoir Characterization: Unconventional Resources Technology Conference, Austin, TX. doi10.15530-urtec-2017, 2670537

Kosanke, T.H., S.E. Perry, and R. Lopez, 2017, Hyperspectral Imaging Technology Development and Application; Implications for Thin-Bedded Reservoir Characterization: AAPG 2017 Annual Convention and Exhibition, Houston, Texas, April 2-5, 2017, Search and Discovery Article #42119 (2017). Website accessed September 2019.

Kurz, T.H., S.J. Buckley, J.A. Howell, and D. Schneider, 2008, Geological Outcrop Modelling and Interpretation using Ground Based Hyperspectral and Laser Scanning Data Fusion: International Archives of the Photogrammetry, Remote Sensing and Spatial Information Sciences, v. 37, p. 1229-1234.

Kurz, T.H., S.J. Buckley, J.A. Howell, and D. Schneider, 2011, Integration of Panoramic Hyperspectral Imaging with Terrestrial LIDAR Data: The Photogrammetric Record, v. 26, p. 212-228.

Lu, G., and B. Fei, 2014, Medical Hyperspectral Imaging: A Review: Journal of Biomedical Optics, v. 19, p. 010901. doi.org/10.1117/1.JBO.19.1.010901

Manea, D., and M. Calin, 2015, Hyperspectral Imaging in Different Light Conditions: The Imaging Science Journal, v. 63, p. 214-219.

Marshall, S., 2011, Hyperspectral Imaging Technology: AWE International, v. 1, p. 9-15.

Monteiro, S.T., R.J. Murphy, F. Ramos, and J. Nieto, 2009, Applying Boosting for Hyperspectral Classification of Ore-bearing Rocks: Machine Learning for Signal Processing XIX - Proceedings of the 2009 IEEE Signal Processing Society Workshop, MLSP 2009, p. 1-6.

Murphy, R.J., and S.T. Monteiro, 2013, Mapping the Distribution of Ferric Iron Minerals on a Vertical Mine Face using Derivative Analysis of Hyperspectral Imagery (430–970nm): ISPRS Journal of Photogrammetry and Remote Sensing, v. 75, p. 29–39.

Plaza, A., J.A. Benediktsson, J.W. Boardman, J. Brazile, L. Bruzzone, G. Camps-Valls, J. Chanussot, M. Fauvel, P. Gamba, and A. Gualtieri, 2009, Recent Advances in Techniques for Hyperspectral Image Processing: Remote Sensing of Environment, v. 113, p. S110-S122.

Sun, D.-W., 2010, Hyperspectral Imaging for Food Quality Analysis and Control: Academic Press, Elsevier, London, ISBN: 9780123747532, 496 p.

Taranik, J., and Z. Aslett, 2009, Development of Hyperspectral Imaging for Mineral Exploration: Reviews in Economic Geology, v. 16, p. 83-95.

Vane, G., and A.F. Goetz, 1988, Terrestrial Imaging Spectroscopy: Remote Sensing of Environment, v. 24, p. 1-29.

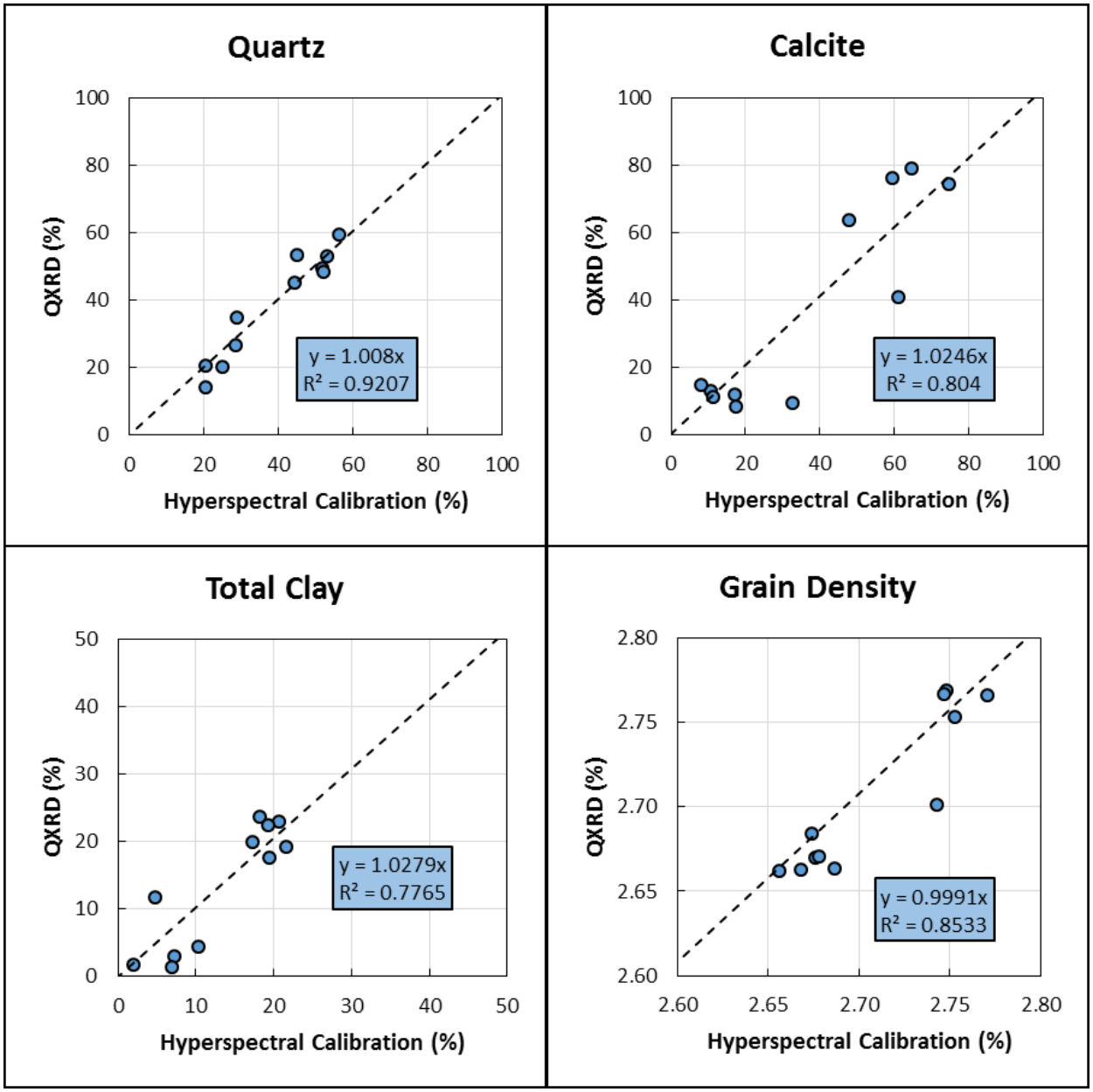

Figure 1. Comparison between the hyperspectral calibrated abundance and XRD measured abundance for the subset of Bone Spring Shale samples.

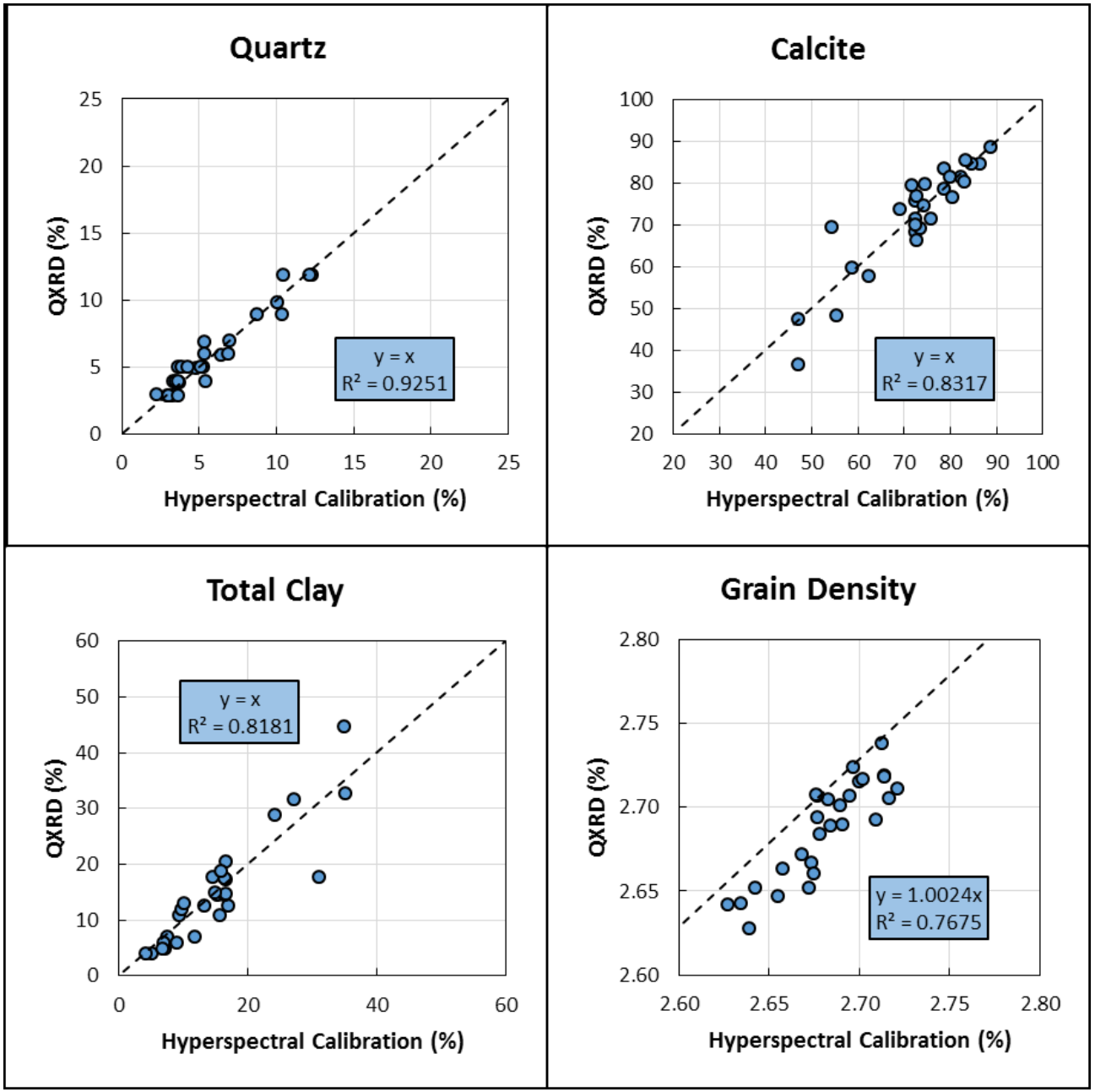

Figure 2. Comparison between the hyperspectral calibrated abundance and XRD measured abundance for the subset of Austin Chalk samples.

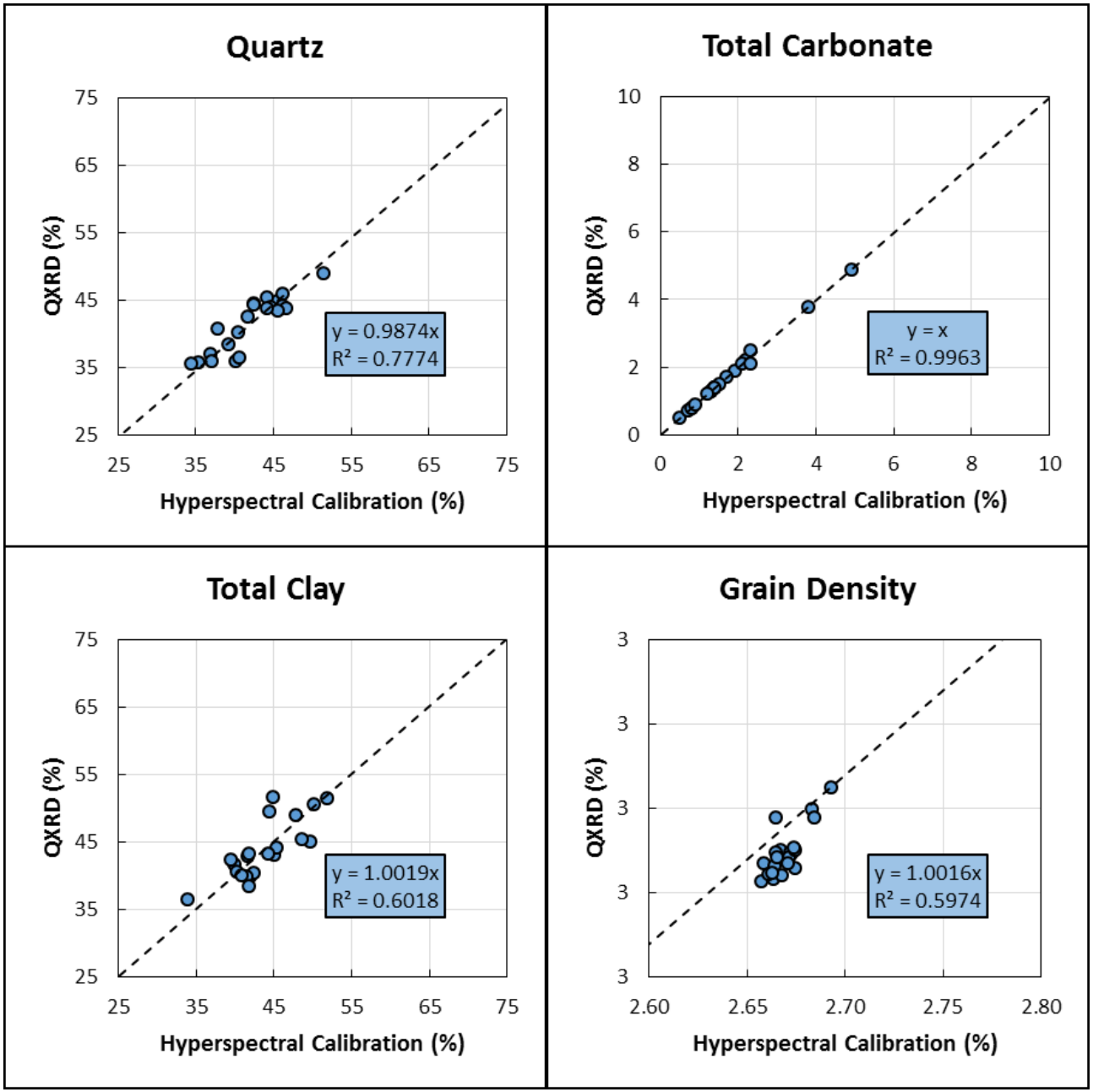

Figure 3. Comparison between the hyperspectral calibrated abundance and XRD measured abundance for the set of Wilcox samples.

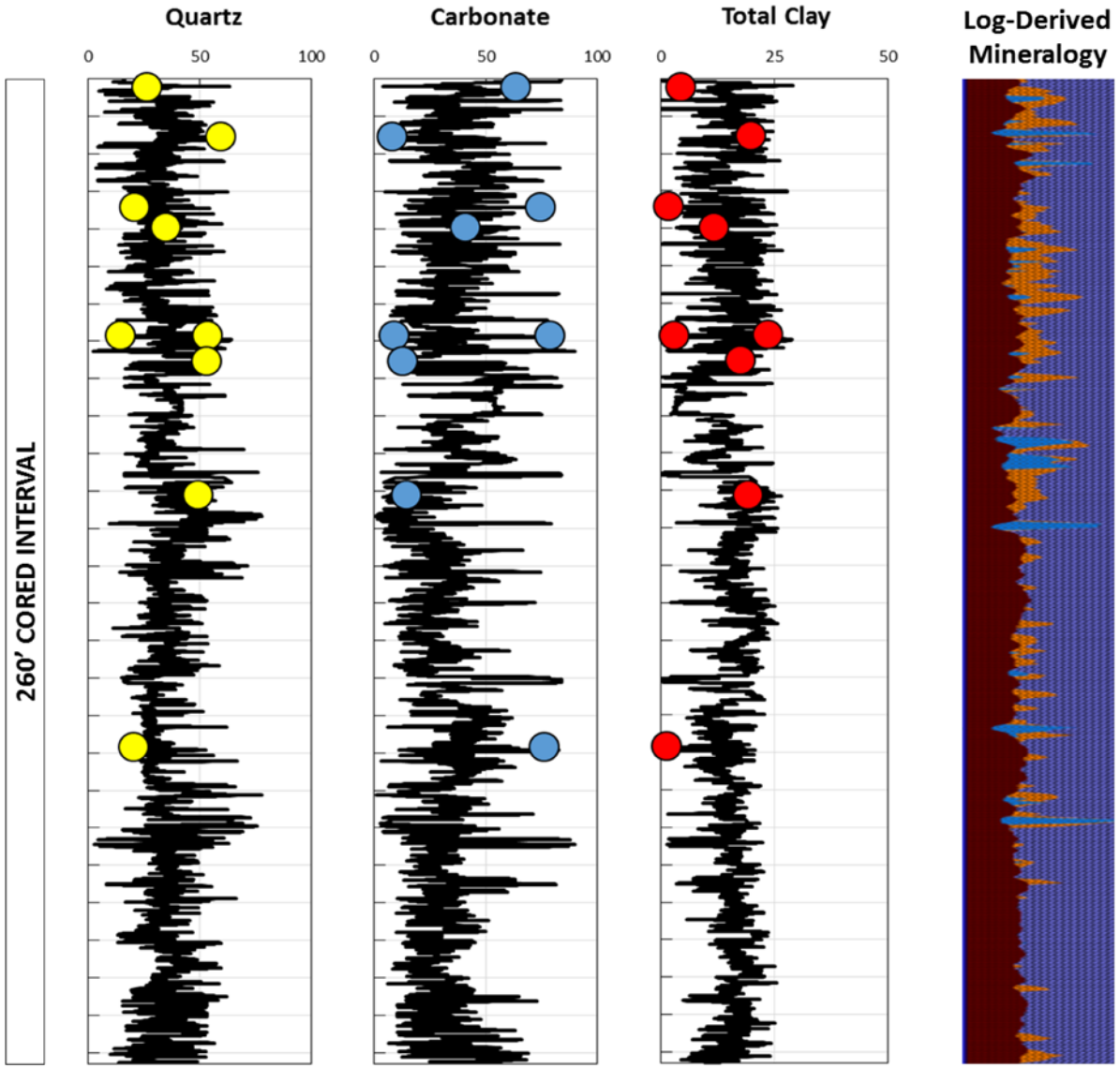

Figure 4. Comparison of hyperspectral-derived continuous mineral logs and wireline-derived mineral log. XRD points used for calibration are displayed as discrete points along the interval. A total of 9 XRD samples were available to use for calibration – additional points would improve calibration accuracy. The resolution of the hyperspectral mineralogy is evident when compared to the log-derived mineralogy as thin interbedded layers are able to be captured.